RSC Advances

PAPER

View Article Online
View Journal | View Issue



Cite this: *RSC Adv.*, 2025, **15**, 45928

# Volume-dependent catalytic efficiency of highly durable Au@Ag–Pt core@multi-shell nanoparticles in methylene blue reduction

Hu-Jun Lee, [ab] Anh Thi Ngoc Dao*[c] and Kenji Kaneko*[a]

Received 27th August 2025
Accepted 10th November 2025

DOI: 10.1039/d5ra06393k

rsc.li/rsc-advances

Monodispersed spherical Au@Ag–Pt core@multi-shell nanoparticles were synthesized using a co-reduction method that integrates galvanic replacement with a versatile reducing agent. Their nanostructure was thoroughly characterized using scanning transmission electron microscopy and energy-dispersive X-ray spectroscopy. The average diameter of the Au core was 18 nm, while the Pt granules within the shell region measured approximately 2.1 nm, with the Ag–Pt shell having an average thickness of 3.3 nm. The catalytic activity of these nanoparticles was evaluated by the reduction of methylene blue dye in the presence of $NaBH_4$, monitored by ultraviolet-visible spectrophotometry. The mass-to-charge ratio peaks of the reduced dye were further quantified using electrospray ionization mass spectrometry. A representative pseudo-first-order rate constant of 5.924 $min^{-1}$ was calculated. Moreover, the nanoparticles maintained over 99% catalytic efficiency even after six consecutive cycles of methylene blue reduction and after six months of storage, with no significant changes in their nanostructure. These results demonstrate the nanoparticles' excellent stability, reusability, and durability. Therefore, Au@Ag–Pt core@multi-shell nanoparticles synthesized *via* this co-reduction approach show strong potential for practical applications in wastewater treatment involving azo dye reduction.



## 1. Introduction

Water pollution remains one of the most critical life-threatening environmental challenges, posing serious short- and long-term threats to human health, including liver and kidney damage, cancer, and other serious diseases.[1] It also endangers ecological safety and biodiversity.[2] Extensive research has been actively conducted to detoxify water pollution sources caused by polycyclic aromatic hydrocarbons (PAHs), such as methylene blue (MB) and methylene orange.[3–8] MB, a highly toxic azo dye with the molecular formula $C_{16}H_{18}ClN_3S$, contains a benzene ring that imparts redox activity.[9–11] Despite its hazardous nature, MB is widely used in industries for dyeing products such as textiles, paper, and leather. Consequently, a vast quantity of MB-containing wastewater is discharged into rivers, soil, and marine environments without adequate treatment, contributing to severe environmental contamination.[12]

Hence, developing a facile, cost-effective, efficient, and environmentally friendly method to eradicate these PAHs from wastewater remains a formidable challenge. Numerous strategies have been proposed for the removal of MB dye from industrial effluents, which can be broadly classified into physical, biological, and chemical approaches, as summarized in Table 1. Physical methods include using carbon nanotubes,[13] activated carbon,[14] zeolites,[15] metal–organic frameworks (MOF),[7] and membrane filtration.[16] Biological approaches primarily involve biodegradation processes,[17] while chemical methods encompass ion exchange resins,[18] photodegradation,[19] chemical oxidation,[20] and catalytic reduction.[21]

Among the various approaches, catalytic reduction using nanoparticles (NPs) has gained considerable attention due to its cost-effectiveness,[22] high reduction efficiency,[23] and environmental sustainability,[24] compared to many other conventional methods.[7,13–20] The exceptional catalytic properties of NPs are primarily attributed to their high surface-to-volume ratio, the abundance of active surface atoms, and their unique electronic structures compared to their bulk form.[25] These characteristics enable enhanced interaction with target molecules, making NPs highly effective for pollutant degradation in wastewater treatment applications.

In particular, the design of novel NPs plays a crucial role in enhancing the catalytic reduction of MB dye.[26] Catalytic materials for NPs can generally be classified into two types: non-noble metals, such as metal oxides[8,27] and sulfides,[28–31] and noble metals including Au,[32] Ag,[22] Pt,[33] and Pd.[23] Extensive studies have focused on developing cost-effective and highly active non-noble metal catalysts, such as Ni/graphene,[34] CoB,[35]

[a]*Department of Materials, Kyushu University, 744 Motooka, Nishi, Fukuoka, 819-0395, Japan. E-mail: kaneko.kenji.513@m.kyushu-u.ac.jp*

[b]*Institute of Advanced Composite Materials, Korea Institute of Science and Technology (KIST), Jeonbuk, 55324, Republic of Korea*

[c]*Graduate School of Integrated Science and Technology, Nagasaki University, 1-14 Bunkyo-machi, Nagasaki, 852-8521, Japan. E-mail: anh.dao@nagasaki-u.ac.jp*

Table 1 Advantages and disadvantages of various methods for removing the MB dye

| Methods | Example | Advantages | Disadvantages | Ref. |
|---|---|---|---|---|
| Physical | Carbon nanotube<br>Activated carbon | No toxic byproducts | High cost<br>Frequent blockage<br>Time-consuming | 7 and 13–16 |
| | Zeolites<br>MOF<br>Membrane filtration | Complete removal | High maintenance cost | |
| Biological | Biodegradation | Environmental-friendly | Low reduction efficiency<br>Incomplete removal | 17 |
| | | No toxic byproducts<br>Low cost | Time-consuming | |
| Chemical | Ion exchange resin | Low cost<br>Simple fabrication | Time-consuming<br>High maintenance cost | 18 |
| | Photodegradation | Environmental-friendly<br>Low cost<br>No toxic byproducts | Incomplete removal<br>Difficulty in reuse<br>Time-consuming | 19 |
| | Chemical oxidation | Renewable sources (sunlight)<br>Complete removal | Nonbiodegradable byproducts<br>Expensive operating setups<br>Comparatively slow reduction | 20 |
| | Catalytic reduction | No toxic byproducts<br>High reduction efficiency<br>Environmental-friendly | High cost of noble metal NPs | 21 |

NiB.[36] While these materials offer economic advantages and show promising catalytic activity, as outlined in Table 2,[8,27–31] their catalytic efficiency remains insufficient for commercial-scale applications. Additionally, their low oxidation resistance leads to poor long-term stability. In contrast, noble metal NPs are highly valued for their exceptional stability, superior catalytic performances, and robust oxidation resistance. These attributes allow for reduced material usage without compromising efficiency, making them attractive candidates for sustainable and reliable wastewater treatment technologies.

Various noble monometallic NPs, including Au,[32] Ag,[22] Pt,[33] and Pd,[23] have been widely used to enhance the reduction of nitrophenols and azo dyes.[37] However, these monometallic NPs are thermodynamically unstable due to their high surface energy, which often causes them to agglomerate and to coalesce during the catalytic reactions. Such structural transformations at the nanoscale often lead to a significant decline in both catalytic activity and selectivity. In contrast, multi-metallic NPs offer enhanced stability, allowing them to maintain catalytic performance over extended periods.[38] For example, Omar *et al.* demonstrated that Au/Ag bimetallic NPs exhibit broadened absorption bands across a wider wavelength compared to monometallic counterparts, thereby improving catalytic performance in the reduction of MB.[39] Similarly, Ma *et al.* reported that Au/Pt nanotriangles with rough surfaces and hollow structures exhibit enhanced photocatalytic activity in reducing *p*-nitrophenol.[40] Moreover, trimetallic NPs have demonstrated various advantages, including improved catalytic activity in Au@AgPd NPs,[41] enhanced antibacterial properties in CuZnFe NPs,[42] extended stability in PtNiCo NPs,[38] and superior selective detectability in Au@PtPd NPs.[43]

In this study, spherical Au@Ag–Pt NPs with core@multi-shell structure were synthesized using the co-reduction method. Their structural and compositional characteristics were thoroughly analyzed using transmission electron microscopy (TEM), high-resolution transmission electron microscopy

Table 2 Catalytic efficiency and cost of NPs of non-noble metal NPs for reducing azo dyes

| No. | Catalyst | Usage | Cost of used quantity | Concentration of azo dye | Reduction efficiency after 6th cycle | $K$ ($min^{-1}$) | Ref. |
|---|---|---|---|---|---|---|---|
| 1 | NiO | 20 mg | $0.0045 | MB, 0.03 mM | 86% | 0.552 | 27 |
| 2 | $TiO_2$ | 100 mg | — | MB, 1 mM | 79% | 0.115 | 8 |
| | | | | MO, 1 mM | — | 0.058 | |
| 3 | BiMnOS | 10 mg | $0.0052 | MB, 0.14 mM | — | 0.283 | 28 |
| | | | | 4-NP, 0.14 mM | 90.6% | 0.351 | |
| 4 | CeCoOS | 10 mg | $0.006 | 4-NP, 0.14 mM | 97.5% | 0.325 | 29 |
| 5 | CuSnOS | 10 mg | $0.0057 | MB, 1 mM | — | 0.721 | 30 |
| | | | | RhB, 1 mM | 92.3% | 1.148 | |
| 6 | CuMoOS | 10 mg | $0.0082 | MB, 0.14 mM | — | 0.524 | 31 |
| | | | | 4-NP, 0.14 mM | 96% | 0.753 | |

(HRTEM), and high-angle annular dark field scanning transmission electron microscopy (HAADF-STEM) with energy dispersive X-ray spectroscopy (EDS). The catalytic activities of the Au@Ag–Pt NPs were investigated using UV-visible (UV-vis), double-beam spectrophotometry and electrospray ionization mass spectrometry (ESI-MS). These techniques enabled precise monitoring of the dye degradation process and provided insights into the reaction kinetics and efficiency of the synthesized nanocatalysts.

## 2. Experimental

### 2.1. Samples

Gold(III) chloride trihydrate ($HAuCl_4 \cdot 3H_2O$, ≥99.9% trace metals basis, Sigma-Aldrich), silver nitrate solution 0.02 M ($AgNO_3$, Sigma-Aldrich), chloroplatinic acid solution (8 wt%, $H_2PtCl_6$, Sigma-Aldrich), sodium citrate tribasic dihydrate ($Na_3C_6H_5O_7 \cdot 2H_2O$, ≥99%, Wako Pure Chemical Industries), sodium borohydride ($NaBH_4$, 99%, Wako Pure Chemical Industries), and methylene blue ($C_{16}H_{18}ClN_3S \cdot 3H_2O$, 98.5%, Wako Pure Chemical Industries) were purchased and used without further modification. Deionized water (18.2 MΩ) was used for all reactions.

### 2.2. Synthesis of Au@Ag–Pt core@multi-shell NPs

The Au@Ag–Pt core@multi-shell NPs were synthesized using the co-reduction method, a combination of galvanic replacement reaction and a versatile reducing agent.[44] Initially, $HAuCl_4$ (20 mM, 0.74 mL) was reduced to form Au NPs using 2.4 mL of 20 mM aqueous trisodium citrate ($Na_3C_6H_5O_7$) under a reflux condition for 60 min. Subsequently, the Ag-shell was grown on the Au NPs by adding 0.88 mL of 20 mM aqueous $AgNO_3$ into the reaction with additional sodium citrate (20 mM, 1.1 mL) and reacted for 20 min. Finally, $H_2PtCl_6$ (20 mM, 0.74 mL) was added, and the reaction continued under the same conditions for another 60 min. All reactions were carried out in one pot, under Ar flow (100 mL $min^{-1}$).

### 2.3. Nanostructural characterizations

The size and shape of the Au@Ag–Pt core@multi-shell NPs were analyzed by transmission electron microscopy (TEM, JEM-2100HC) operated at acceleration voltages of 200 kV. Structural information of these NPs was obtained through the selected area electron diffraction pattern (SAEDP). Furthermore, high-angle annular dark-field (HAADF) imaging was conducted by scanning transmission electron microscopy (STEM; JEOL ARM-200F) to confirm the presence of Ag and Pt in the multi-shell region. Elemental distribution maps from NPs were acquired using a combination of STEM and energy-dispersive X-ray spectroscopy (EDS) analyses.

### 2.4. Catalytic activity study

The catalytic activities of Au@Ag–Pt NPs were investigated by measuring the reduction of MB dye by sodium borohydride ($NaBH_4$). 5 mL of MB (0.1 mM) dye and 0.5 mL of $NaBH_4$ (0.05 M) solutions were mixed, followed by the addition of solution with Au@Ag–Pt NPs (0.10, 0.20, 0.30, 0.35, 0.40 mL, 0.01 mM). All reactions were performed in a 25 mL glass vial under atmospheric conditions with magnetic stirring to ensure homogeneous mixing. UV-visible double-beam

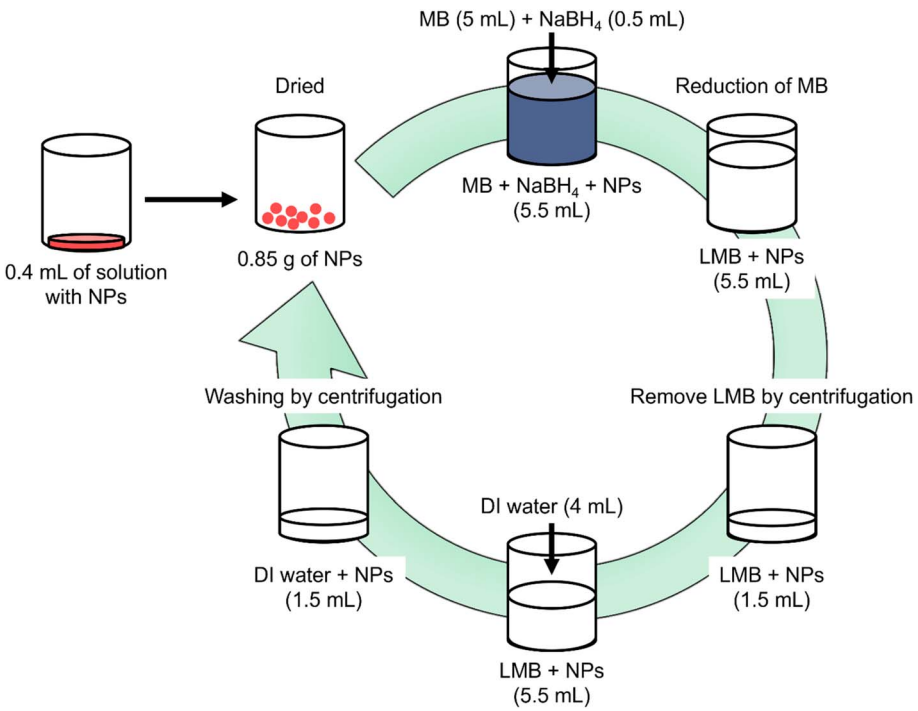


Fig. 1 A schematic diagram of cycle tests of 0.4 mL of solution with NPs.

spectrophotometer (UV-vis spectrophotometer, JASCO, V-670) was used to monitor the reaction progress by recording the time-dependent UV-vis absorption spectra of the mixtures at 664 nm in a quartz cuvette (path length 1 mm). For comparison, a similar procedure was carried out to examine the reduction of MB dye by $NaBH_4$ without NPs. Scanning of various samples was performed in the range of 200–800 nm at room temperature 25 °C, and the reduction efficiency was measured using the following equation:

$$\text{Reduction efficiency of MB dye } [\%] = \frac{A_0 - A_f}{A_0} \times 100 \quad (1)$$

where $A_0$ represents the initial absorbance of MB dye before the reaction, while $A_f$ is the final absorbance of MB dye after the reaction.

In this catalytic process, the concentration of $NaBH_4$ was excessive compared to the amount of MB dye, causing the reaction to follow pseudo-first-order kinetics (molar ratios of $NaBH_4 : MB = 50 : 1$). Therefore, the reaction rate was measured using pseudo-first-order kinetics to evaluate the catalytic activity efficiency of the Au@Ag–Pt NPs, and the apparent rate constant, $k$, was obtained using the following equation:

$$kt = -\ln\left(\frac{A_t}{A_0}\right) \quad (2)$$

where, $A_t$ denotes the absorbance of characteristic peaks of MB at reaction time $t$. In addition, the 0.4 mL of solution with NPs were dried on a hot plate (120 °C), yielding 0.85 mg of NPs, as shown in Fig. 1. UV-vis data was performed across six reaction cycles, and ESI-MS to evaluate the stability and reusability of the NPs. The durability of NPs was also examined by the UV-vis studies after storage for six months at room temperature (25 °C) under atmospheric conditions, during which three independent stability tests were carried out to confirm the long-term preservation of their catalytic performance.

### 2.5. Quantification of LMB by ESI-MS

The leuco-MB (LMB) generated by the reduction of MB was identified using a high-resolution quadrupole time-of-flight mass spectrometer (QTOF-MS, micrOTOF-Q III, Bruker, USA). The ESI source in the positive mode helps separate MB and LMB based on their mass-to-charge ($m/z$) ratio. A syringe pump with a flow rate of 20 μL $min^{-1}$ was used to introduce the sample solution into the ESI source for analysis, with the following electrospray conditions: capillary voltage, 4500 V; nebulizer pressure, 0.3 bar; drying gas temperature, 180 °C; $N_2$ drying gas, 4 L $min^{-1}$.

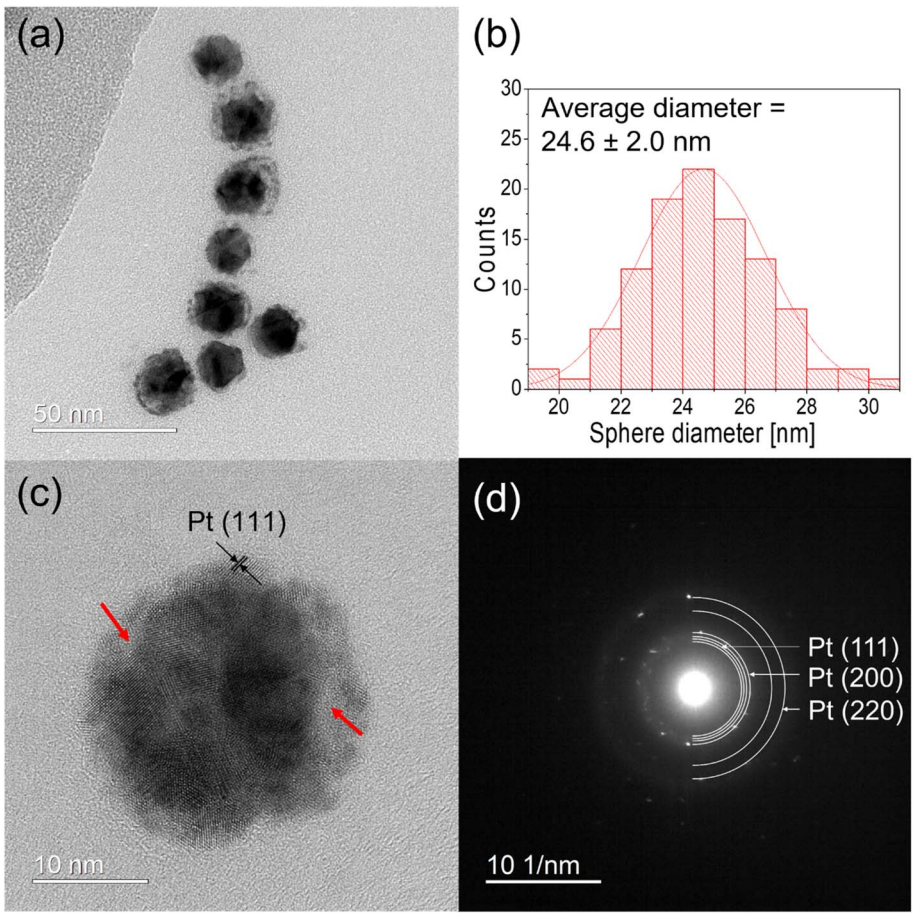


Fig. 2 (a) A representative TEM image, (b) the distribution of the average diameter of NPs, (c) HRTEM image of NPs, and (d) SAEDP image corresponding to (c).

# 3. Results and discussion

## 3.1. Characterization of NPs

As shown in Fig. 2(a), the TEM image of the NPs reveals three distinctive contrast regions. A relatively large dark core, surrounded by a composed of dark granular features and bright film-like layer. The average diameter of the NPs was measured to be 24.6 ± 2.0 nm as shown in Fig. 2(b).

The HRTEM image of a representative NP in Fig. 2(c) displays lattice fringes corresponding to the Pt(111) plane within the granular contrast region, as indicated by a black arrow. Due to the nearly identical lattice spacings of the Au(111) and Ag(111), $a_{Au} = 2.355$ Å and $a_{Ag} = 2.359$ Å, distinguishing between them using HRTEM is challenging. Additionally, regions without lattice fringes indicated by red arrows in Fig. 2(c), suggest the presence of randomly distributed voids.

Selected-area electron diffraction patterns (SAEDPs), obtained from the same region shown in Fig. 2(c), exhibit multiple concentric ring characteristics of face-centered cubic (FCC) structures, as shown in Fig. 2(d). The unlabeled rings in Fig. 2(d) correspond to (111), (200), and (220) planes of either Au or Ag.

Annular bright-field (ABF) STEM imaging provides detailed insights into the structural characteristics of the synthesized Au@Ag–Pt NPs, confirming their core@multi-shell morphology, as shown in Fig. 3. In low-magnification images, the central Au core appears dark due to its higher atomic number, while the surrounding Ag–Pt multi-shell appears relatively lighter contrast, as seen in Fig. 3(a) and (c). High-magnification images reveal additional structural features, including internal voids within the Ag–Pt multi-shell, as shown in Fig. 3(b) and (d). These voids, attributed to the Kirkendall effect occurring during synthesis, result from the unequal diffusion rates of metal atoms. The presence of these voids is expected to enhance catalytic performance by increasing the active surface area and improving reactant accessibility to Pt catalytic sites.

ABF-STEM imaging further indicates that Ag and Pt do not form a homogeneous alloy but instead create a distinct multi-shell structure. This observation is supported by contrast variations within the shell region, as shown in Fig. 3(a) and (c). This unique structural configuration is particularly significant, as it ensures that Pt remains exposed at the surface, thereby maximizing its catalytic accessibility, while the Ag–Pt shell provides mechanical stability. The strategic distribution of Pt granules within the shell optimizes the usage of Pt, enhancing catalytic activity. Moreover, the Ag–Pt multi-shell acts as a protective barrier, shielding the Au core from direct exposure to the reaction environment. This prevents core dissolution or structural degradation during repeated catalytic cycles. Furthermore, the voids observed within the shell accommodate volumetric changes during catalytic reactions, thereby preventing the

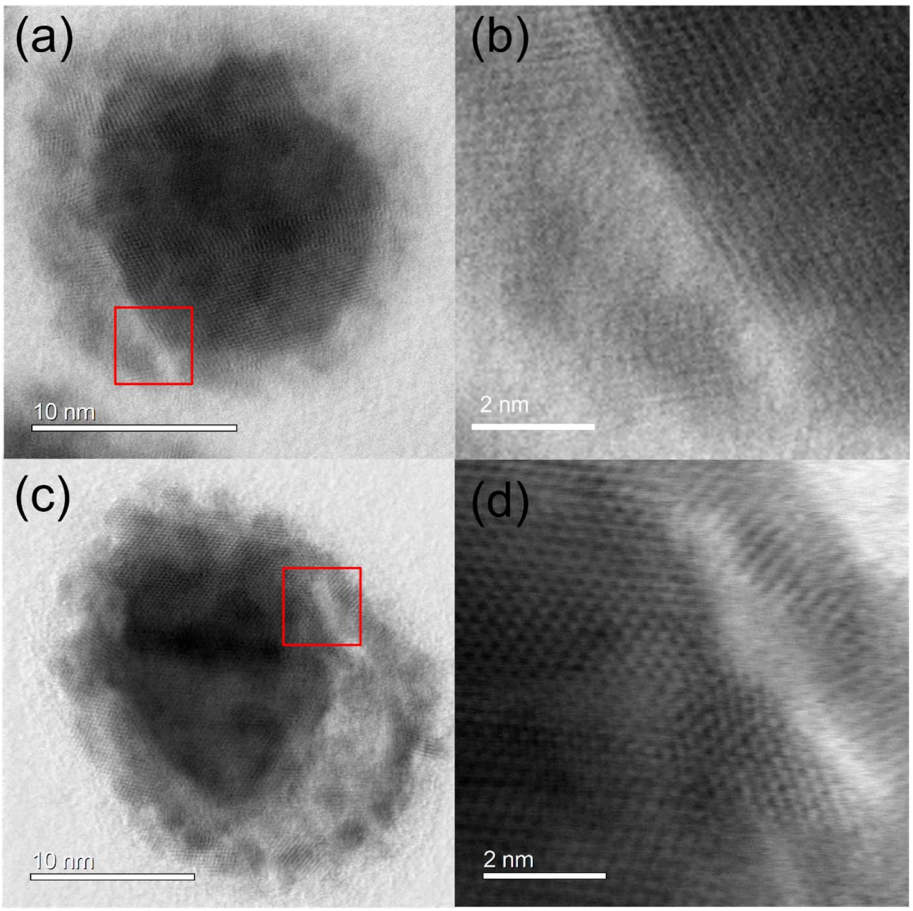


Fig. 3 Annular bright-field STEM images of NPs. (a and c) Low-magnification images and (b and d) high-resolution images.

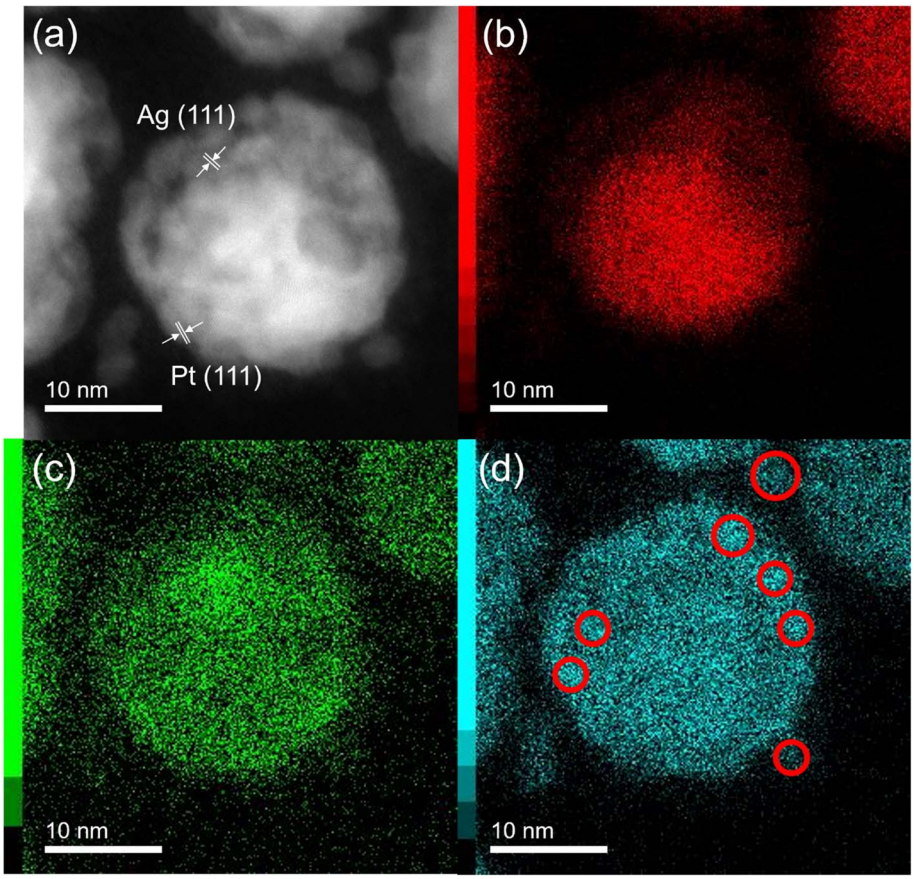


Fig. 4 (a) HAADF-STEM image, elemental distribution maps of (b) Au L, (c) Ag L, and (d) Pt L of Au@Ag–Pt core@multi-shell NPs where Au L, Ag L, and Pt L were pseudo-colored in red, green, and cyan, respectively.

collapse or aggregation of NPs. This structural adaptability contributes to the long-term durability and reusability of the Au@Ag–Pt NPs in practical applications.

High-angle annular dark-field scanning transmission electron microscopy (HAADF-STEM), combined with EDS, was employed to analyze the elemental distribution of the synthesized Au@Ag–Pt NPs, as shown in Fig. 4. Comparative analysis of the images revealed lattice fringes corresponding to the Ag(111) and Pt(111) planes within the shell region, as shown in Fig. 4(a), with the outermost shell exhibiting a granular distribution of Pt. The successful synthesis of Au@Ag–Pt core@multi-shell NPs *via* the co-reduction method was conclusively demonstrated through the elemental distribution maps, shown in Fig. 4(b)–(d). These maps confirmed that the core composed of Au, while the multi-shell was composed of a mixture of Ag and Pt. The granular nature of Pt was further validated by the elemental distribution map of Pt in Fig. 4(d), where red circles highlighted the Pt granules distributed within the image.

### 3.2. UV-vis spectrophotometer analysis

The catalytic reduction performance of the Au@Ag–Pt NPs was evaluated through the conversion of the MB into LMB, a less toxic substance,[26] using $NaBH_4$ as the reducing agent. UV-vis absorption spectra for MB dye reduction were recorded in the absence of both NPs and $NaBH_4$ to confirm the catalytic role of Au@Ag–Pt NPs, as shown in Fig. 5(a) and (b). The UV-vis spectrum of the MB solution revealed characteristic absorption peaks at 664 nm ($\pi$–$\pi^*$) and 612 nm (n–$\pi^*$).[45] In the absence of NPs, the reduction rate of the MB dye was notably slow, with the characteristic peak at 664 nm peak remaining prominent even after 60 minutes, as shown in Fig. 5(a). Similarly, in the absence of $NaBH_4$, the 664 nm absorption peak remained nearly unchanged, indicating that no reduction occurred between MB and Au@Ag–Pt NPs alone, as shown in Fig. 5(b). These findings confirm that both NPs and $NaBH_4$ are essential for initiating and sustaining the catalytic reduction of MB to LMB; with the NPs serving as catalysts to activate the reaction. Further UV-vis spectra were recorded using varying volumes of NPs, ranging from 0.10 to 0.40 mL, to investigate the influence of NP concentration on reaction kinetics, as shown in Fig. 5(c)–(g). In all cases, the reduction reaction was completed within 1 minute, and a progressive decrease in the absorption peak at 664 nm was observed with increasing NP concentration, indicating enhanced catalytic activity.

The reduction efficiency of MB dye increased progressively with the higher concentration of Au@Ag–Pt NPs, as shown in Fig. 5(h), (i), and S2. However, when the NP volume ranged between 0.10 and 0.35 mL, the reduction of MB dye remained

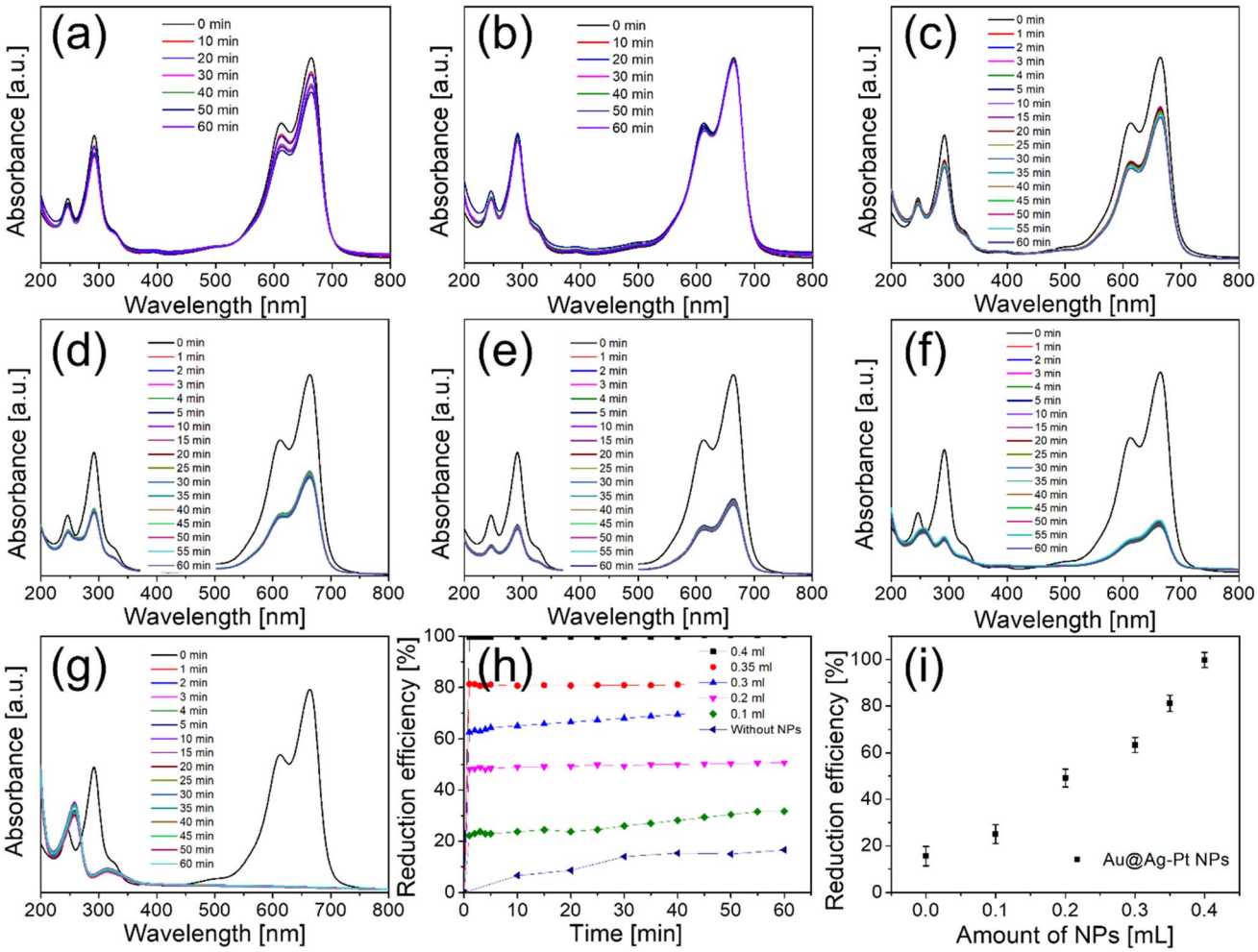


Fig. 5 The UV-vis absorption spectra illustrating the reduction of MB dye under different conditions: (a) without Au@Ag–Pt NPs, (b) without $NaBH_4$ but with varying volumes of Au@Ag–Pt NPs: (c) 0.10 mL, (d) 0.20 mL, (e) 0.30 mL, (f) 0.35 mL, (g) 0.40 mL, and (h and i) the corresponding reduction efficiency after 60 minutes.

incomplete due to an insufficient amount of catalyst.[46] Notably, the characteristic peak of LMB at 260 nm was absent in samples with NP volumes between 0.10 and 0.30 mL, indicating incomplete conversion. The reusability of the NPs was confirmed through UV-vis measurements conducted over six consecutive cycles of MB reduction, as shown in Fig. 6. Remarkably, the catalytic efficiency remained above 99%, even after six months of storage at room temperature (25 °C) under ambient pressure, 1 atm. These results demonstrate excellent stability, durability, and reusability of the Au@Ag–Pt NPs,

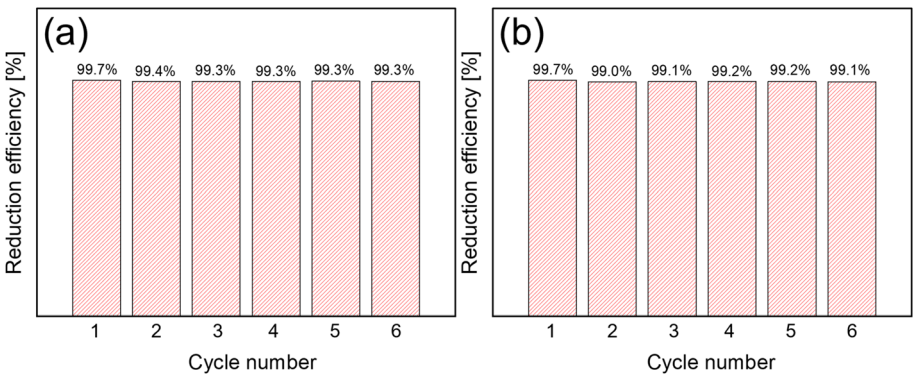


Fig. 6 Recycling activity of (a) 0.4 mL of solution with initial NPs and (b) after 6 months.

Table 3 A comparison of the catalytic activity of the NPs used in this experiment with those of other studies on the MB reduction reaction

| No. | Catalyst | Dye | Reducing agent | Reduction efficiency after 60 minutes | $K$ ($min^{-1}$) | Ref. |
|---|---|---|---|---|---|---|
| 1 | Au@Ag–Pt NPs, 0.01 mM | MB, 0.1 mM | $NaBH_4$, 0.05 M | 99.7% | 5.924 | This study |
| 2 | Au NPs, 0.5 mM | MB, 1 mM | $NaBH_4$, 0.1 M | 80% | 0.052 | 48 |
| 3 | Ag NPs, 0.5 mM | MB, 1 mM | $NaBH_4$, 0.1 M | 80% | 0.042 | 48 |
| 4 | Pt NPs, 0.5 mM | MB, 1 mM | $NaBH_4$, 0.1 M | 98% | 0.392 | 48 |
| 5 | Au/Ag (1 : 1) NPs, 0.3 mM | MB, 0.1 mM | $NaBH_4$, 0.05 M | 99% | 0.721 | 45 |
| 6 | Au@Pt NPs, 0.05 mM | MB, 0.05 mM | $NaBH_4$, 0.5 M | 99% | 0.700 | 49 |
| 7 | Au@AgPt alloy NPs, 1.5 mM | MB, 0.05 mM | $NaBH_4$, 0.5 M | 93% | 0.670 | 50 |

making them promising candidates for long-term applications in wastewater treatment.

The catalytic activity of the Au@Ag–Pt NPs was compared with the pseudo-first-order rate constants reported in previously studies on MB dye reduction under comparable experimental conditions, as summarized in Table 3. The Au@Ag–Pt NPs demonstrated outstanding catalytic efficiency, achieving the fastest reduction rate among all reported NPs-based catalysts for MB dye. The enhanced catalytic performance is likely attributed to the synergistic interaction between Ag and Pt within the multi-shell structure, which promotes electron transfer and increases the number of active catalytic sites.[47] In

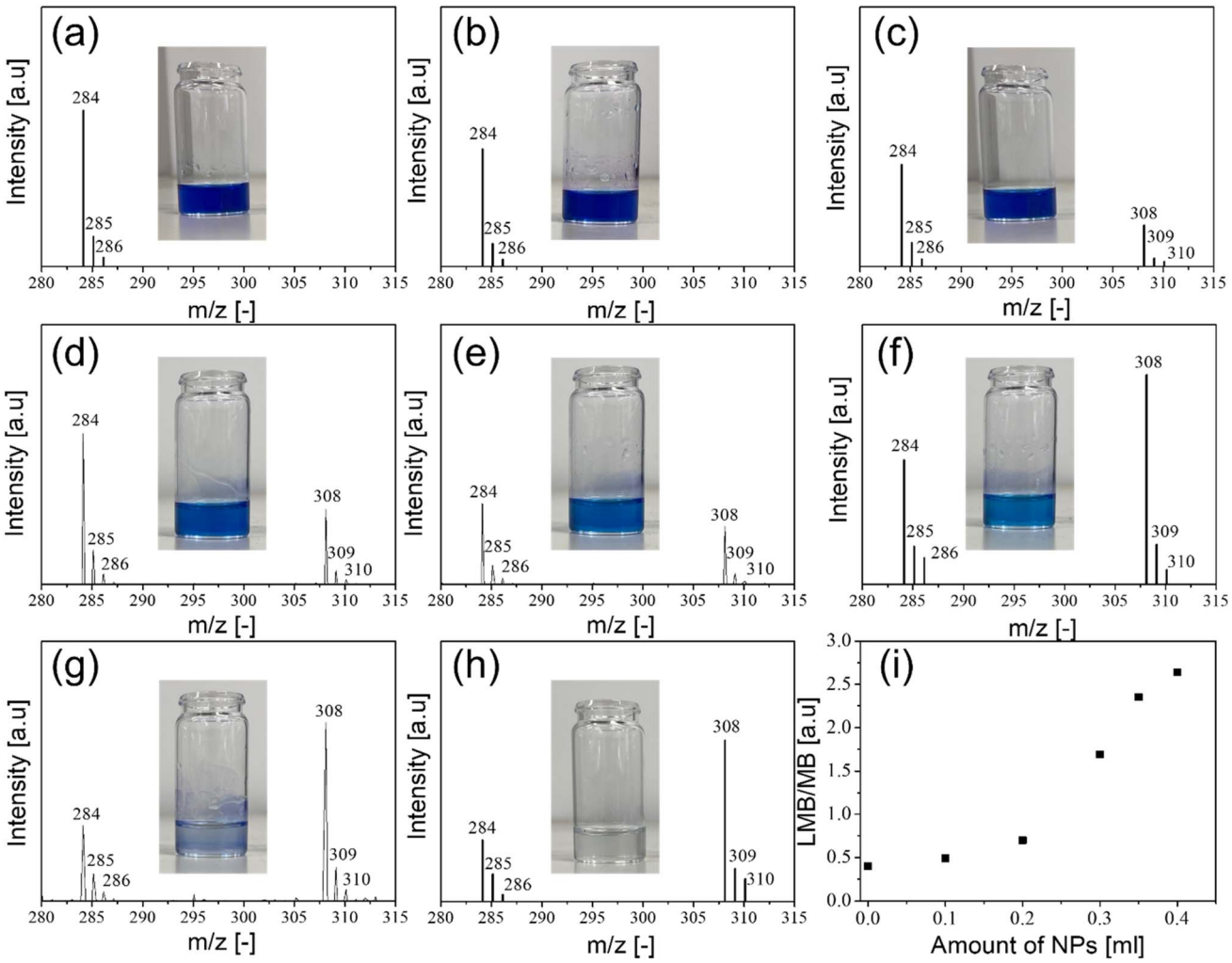


Fig. 7 The ESI-MS in the positive mode for (a) pure MB, (b) pure MB with NPs (0.4 mL), (c) pure MB with $NaBH_4$, and pure MB containing $NaBH_4$ with various amounts of Au@Ag–Pt NPs: (d) 0.10 mL, (e) 0.20 mL, (f) 0.30 mL, (g) 0.35 mL, (h) 0.40 mL. (i) Is the $m/z$ ratio of LMB/MB measured for various amounts of Au@Ag–Pt NPs. The inset images show the gradual color changes from the MB to the reduced MB (LMB) due to the reduction of MB, as seen in (i).

addition, the cost of the used quantity of Au@Ag–Pt NPs was \$0.013, which is approximately twice the cost of non-noble metal NPs reported by Wu *et al.*[31] Despite the higher cost, the Au@Ag–Pt NPs maintained outstanding stability and high catalytic activity, even after six months of storage, underscoring their potential for long-term and practical applications in wastewater treatment.

### 3.3. Electrospray ionization mass spectrometry (ESI-MS) analysis

ESI-MS was employed in positive ion mode to qualitatively identify LMB, the reduced forms of MB following 60 minutes of catalytic reaction, as shown in Fig. 7. In the pure MB solution, as seen in Fig. 7(a), three primary peaks were observed at mass-to-charge ($m/z$) values of 284, 285, and 286. The dominant peak at $m/z = 284$ corresponded to MB in its cationic form $[C_{16}H_{18}N_3S]^+$, while the peaks at 285 and 286 represented heavier isotopic variants, $[^{13}C^{12}C_{15}H_{18}N_3S]^+$ and $[C_{16}H_{18}N_3{}^{34}S]^+$, respectively. In the sample containing pure MB and 0.4 mL of NPs, the $m/z$ ratio of 284/285/286 = 100/19.2/6.0, remained consistent with that of pure MB, due to the absence of electron donation by $NaBH_4$ and reduction, as seen in Fig. 7(b). In the sample without NPs, additional peaks at $m/z$ = 308, 309, and 310 were detected, corresponding to sodium adducts of LMB, $[C_{16}H_{19}N_3S + Na^+]^+$, $[^{13}C^{12}C_{15}H_{19}N_3S + Na^+]^+$, and $[C_{16}H_{19}N_3{}^{34}S + Na^+]^+$, respectively, as seen in Fig. 7(c). Since LMB is $C_{16}H_{19}N_3S$ and neutral, it is only detectable in positive mode when forming adducts with either a proton ($H^+$) or sodium ion ($Na^+$). Fig. 7(d)–(h) show the ESI-MS spectra obtained by incrementally increasing the NP concentrations from 0.10 to 0.40 mL. The intensity of the $m/z$ = 308 peak, corresponding to LMB, increased proportionally with the decrease in $m/z$ = 284, corresponding to MB, indicating progressive conversion. The LMB/MB ratio for each NP concentration are summarized in Table 4, with values of 0.40, 0.50, 0.71, 1.69, 2.35, and 2.64 for 0, 0.10, 0.20, 0.30, 0.35, 0.40 mL, respectively, as shown in Fig. 7(i). A substantial increase in the $m/z$ ratio was observed starting at 0.30 mL, indicating that at least this volume of NPs is required for effective MB reduction, with complete conversion achieved at 0.40 mL. In addition, despite the completion of reduction, as seen in Fig. 7(h), residual MB peaks persisted in the ESI-MS spectra, suggesting that oxidation of LMB back to MB may occur during the ionization process, a known phenomenon in ESI-MS analysis.

### 3.4. Durability of Au@Ag–Pt core@multi-shell NPs

The durability of the Au@Ag–Pt NPs was evaluated by comparing their nanostructures observed using HAADF-STEM imaging and elemental distribution overlay maps after one cycle, six cycles, and six months of storage (following six cycles) of MB reduction reactions, as shown in Fig. 8. Remarkably, the NPs retained their structural integrity throughout repeated catalytic cycles and prolonged storage. Both low- and high-magnification HAADF-STEM images revealed the preservation of the core@multi-shell morphology, with the Au in the core remaining intact and the Ag–Pt shell remaining its structure. The elemental distribution maps consistently showed distinct localization of Ag and Pt in the shell and Au in the core, validating the stability of the multi-shell architecture. Additionally, individual Pt granules remained well-dispersed on the shell surface, even after extended use. Energy-dispersive X-ray spectroscopy (EDS) analysis further supported these observations, revealing consistent atomic ratios of Ag and Pt relative to Au across all samples, as summarized in Table 5. These results demonstrate the excellent structural and compositional stability of the Au@Ag–Pt NPs, confirming their suitability for long-term catalytic applications.

### 3.5. Catalytic reduction mechanism of MB dye

In the reduction reaction system of MB dye, $NaBH_4$ acts as the electron donor, MB serves as the electron acceptor, and Au@Ag–Pt NPs function as the catalyst, respectively. When $NaBH_4$ is introduced into the reaction medium, it decomposes to produce hydrogen ions ($H^+$) and electrons ($e^-$) in water, which facilitate the reduction of MB to LMB by transferring electrons. The overall reaction is drawn schematically as shown in Fig. 9, and the corresponding chemical equation can be described as follows:

$$NaBH_4 + H_2O \rightarrow Na[BH_3(OH)] + 2H^+ + 2e^- \quad (3)$$

$$C_{16}H_{18}ClN_3S\ (MB) + H^+ + e^- \rightarrow C_{16}H_{19}N_3S\ (LMB) + Cl^- \quad (4)$$

These electron transfer process enhances the reduction efficiency of MB dye, thereby improving the overall catalytic efficiency.

Table 4 The relative $m/z$ ratio of MB (at 284, 285, 286) and LMB (308, 309, 310) peaks depending on the amounts of NPs

| Sample | MB ($m/z$ at 284/285/286) | LMB ($m/z$ at 308/309/310) | $\frac{\text{LMB } (m/z \text{ at } 308)}{\text{MB } (m/z \text{ at } 284)}$ |
|---|---|---|---|
| MB | **100**/19.0/5.7 | N/A | 0 |
| MB + 0.40 mL | **100**/19.2/6.0 | N/A | 0 |
| MB + $NaBH_4$ | **100**/23.0/7.2 | **40.3**/8.0/4.1 | 0.40 |
| MB + $NaBH_4$ + 0.10 mL | **100**/22.6/7.1 | **49.5**/9.1/3.1 | 0.50 |
| MB + $NaBH_4$ + 0.20 mL | **100**/23.5/6.9 | **70.8**/13.1/3.9 | 0.71 |
| MB + $NaBH_4$ + 0.30 mL | **59.3**/18.0/12.5 | **100**/18.8/6.9 | 1.69 |
| MB + $NaBH_4$ + 0.35 mL | **42.5**/15.5/5.2 | **100**/18.8/6.4 | 2.35 |
| MB + $NaBH_4$ + 0.40 mL | **37.9**/16.6/4.0 | **100**/20.1/13.7 | 2.64 |

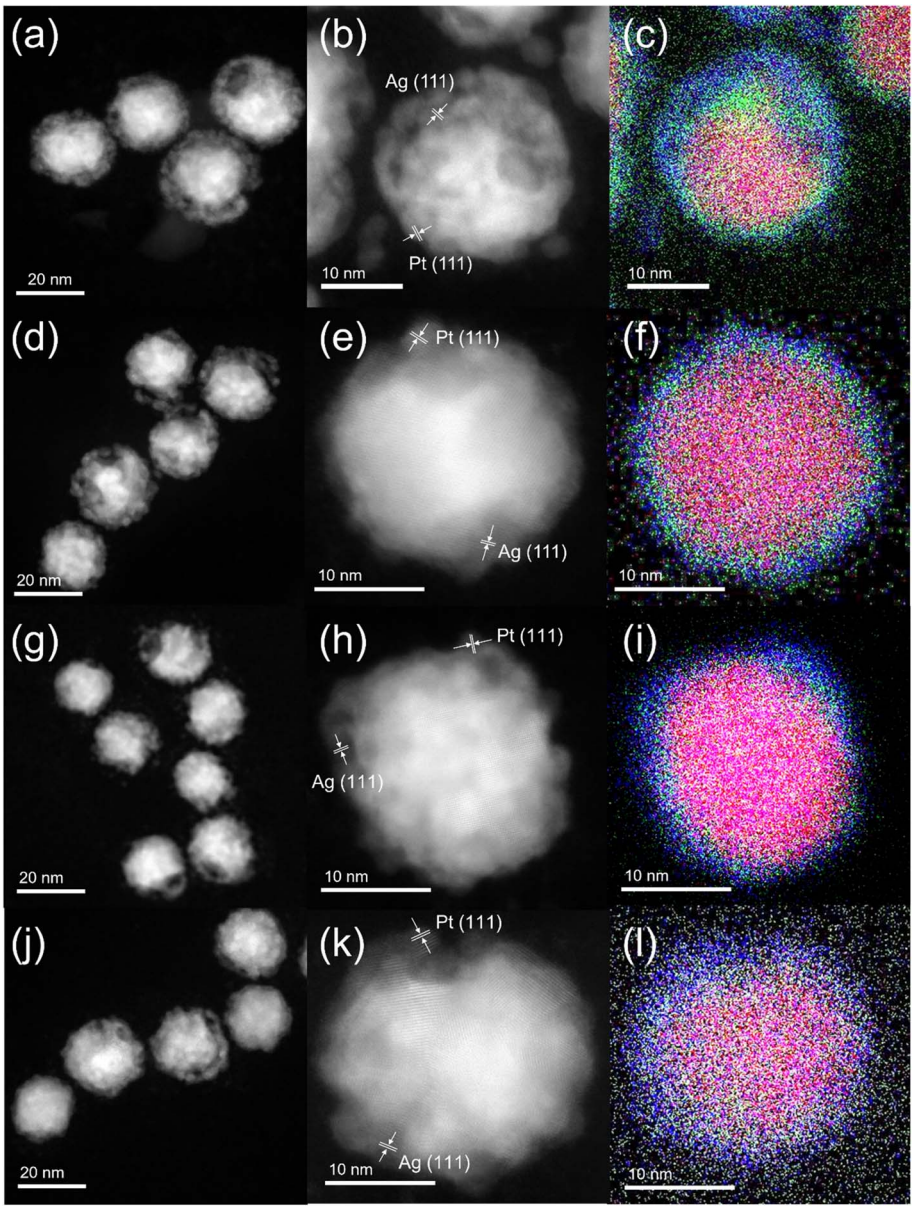


Fig. 8 Sets of HAADF-STEM low- and high-magnified images with elemental distribution overlay maps by STEM-EDS: initial (a–c), after one cycle reaction (d–f), after six cycle reactions (g–i), and after six cycle reactions after 6 months (j–l). The elemental distribution by Au-L, Ag-L, and Pt-L edges were pseudo-colored in red, green, and blue, intentionally.

Table 5 Atomic ratios of Ag/Au and Pt/Au before the MB reduction reaction, one cycle reaction, six cycle reactions, and six cycle reactions after 6 months, respectively

| | Before the MB reduction reaction | After the MB reduction reaction (1 cycle) | After the MB reduction reaction (6 cycles) | MB reduction reaction after 6 months (6 cycles) |
|---|---|---|---|---|
| Ag/Au | 0.69 ± 0.04 | 0.70 ± 0.03 | 0.69 ± 0.05 | 0.69 ± 0.06 |
| Pt/Au | 0.40 ± 0.01 | 0.39 ± 0.04 | 0.38 ± 0.05 | 0.38 ± 0.04 |

Three possible mechanisms have been proposed to explain the rapid reduction of MB in the presence of Au@Ag–Pt NPs. One possible mechanism is that the Ag–Pt multi-shell region contains randomly distributed voids within the matrix of Ag and fine Pt granules. This configuration provides a significant specific surface area of Pt, increasing the number of active catalytic sites and enhancing reaction efficiency. Another possible mechanism is that Ag has a lower work function than

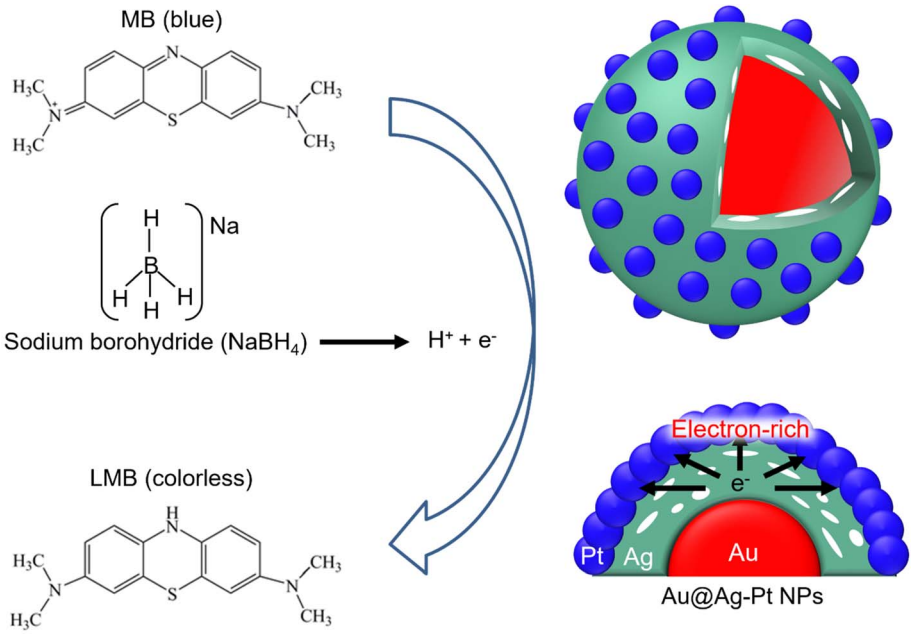


Fig. 9 The schematic diagram of the probable MB reduction mechanism in the presence of the Au@Ag–Pt NPs and $NaBH_4$.

Pt (Ag = 4.26 eV, Pt = 5.65 eV,[51]), allowing electrons from Ag to rapidly transfer to Pt at the Ag/Pt interface. This results in electron-rich Pt, which promotes efficient electron transfer to MB molecules and significantly contributes to the reduction of MB. This synergistic effect of Ag and Pt is schematically illustrated in Fig. 9. Consequently, Au@Ag–Pt NPs facilitate the fast reduction of MB dye due to the substantial active surface area. The other possible mechanism is that the surficial Pt granules play a vital role in hydrogen activation, as schematically shown in Fig. 10, where $NaBH_4$ is adsorbed onto the Pt surface granules and undergoes stepwise dissociation, producing hydrogen ions and electrons through the following reactions:[52]

$$NaBH_4 + H_2O \rightarrow Na[BH_3(OH)] + 2H^+ + 2e^- \quad (5)$$

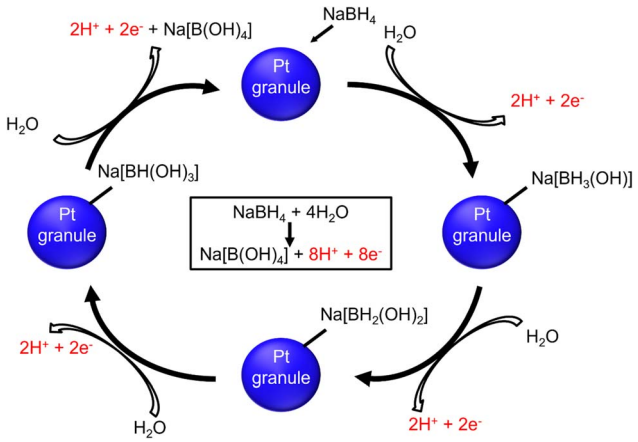


Fig. 10 Mechanism of the hydrolysis of sodium borohydride as catalyzed by the surficial Pt granule.

$$Na[BH_3(OH)] + H_2O \rightarrow Na[BH_2(OH)_2] + 2H^+ + 2e^- \quad (6)$$

$$Na[BH_2(OH)_2] + H_2O \rightarrow Na[BH(OH)_3] + 2H^+ + 2e^- \quad (7)$$

$$Na[BH(OH)_3] + H_2O \rightarrow Na[B(OH)_4] + 2H^+ + 2e^- \quad (8)$$

These activated hydrogen atoms donate electrons to the MB, facilitating its reduction to LMB. The catalytic activation of hydrogen on Pt significantly accelerates the reaction rate compared to the use of $NaBH_4$ alone. In summary, the Au@Ag–Pt NPs contributed to the rapid reduction of MB dye is attributed to the large active surface area, synergistic interaction between Ag and Pt, and efficient hydrogen activation on Pt granules, making Au@Ag–Pt NPs highly effective catalysts for dye degradation.

## 4. Conclusion

Au@Ag–Pt core@multi-shell NPs were synthesized *via* a co-reduction method that combines GRR with chemical reduction. Structural and compositional analysis using STEM and EDS confirmed the formation of NPs with a well-defined core@multi-shell architecture. The catalytic performance of the NPs was validated through UV-vis spectrophotometry and ESI-MS, demonstrating efficient reduction of MB dye to LMB. Optimal catalytic efficiency was achieved with 0.4 mL of NP solution, completing the reduction within 1 minute and yielding a pseudo-first-order rate constant of $5.924 \pm 0.132\ min^{-1}$. The NPs retained over 99% catalytic efficiency after six reaction cycles and six months of storage, with no observable changes in their nanostructures, confirming their exceptional stability, reusability, and durability.

The enhanced catalytic performance is attributed to the synergistic interaction between Ag and Pt within the multi-shell structure, which increases surface area and promotes electron transfer. Combined with their rapid reaction kinetics and long-term stability, Au@Ag–Pt NPs present a promising solution for commercial applications in the treatment of organic pollutants in wastewater.

## Author contributions

Hu-Jun Lee: investigation, data curation, formal analysis, writing – original draft. Anh Thi Ngoc Dao and Kenji Kaneko: conceptualization, methodology, data curation, formal analysis, resources, funding acquisition, writing – review and editing, supervision.

## Conflicts of interest

There are no conflicts to declare.

## Data availability

The datasets generated during and/or analyzed during the current study are available from the corresponding author on reasonable request.

Supplementary information is available. See DOI: https://doi.org/10.1039/d5ra06393k.

## References

1 L. Lin, H. Yang and X. Xu, Effects of Water Pollution on Human Health and Disease Heterogeneity: A Review, *Front. Environ. Sci.*, 2022, **10**, 880246, DOI: 10.3389/fenvs.2022.880246.

2 I. Khan, K. Saeed, I. Zekker, B. Zhang, A. H. Hendi, A. Ahmad, S. Ahmad, N. Zada, H. Ahmad, L. A. Shah, T. Shah and I. Khan, Review on Methylene Blue: Its Properties, Uses, Toxicity and Photodegradation, *Water*, 2022, **14**, 242, DOI: 10.3390/w14020242.

3 N. Sahiner, S. Sagbas and N. Aktas, Very fast catalytic reduction of 4-nitrophenol, methylene blue and eosin y in natural waters using green chemistry: P(tannic acid)-Cu ionic liquid composites, *RSC Adv.*, 2015, **5**, 18183–18195, DOI: 10.1039/c5ra00126a.

4 Q. Li, Y. Li, X. Ma, Q. Du, K. Sui, D. Wang, C. Wang, H. Li and Y. Xia, Filtration and adsorption properties of porous calcium alginate membrane for methylene blue removal from water, *Chem. Eng. J.*, 2017, **316**, 623–630, DOI: 10.1016/j.cej.2017.01.098.

5 K. Naseem, R. Begum, W. Wu, A. Irfan, A. G. Al-Sehemi and Z. H. Farooqi, Catalytic reduction of toxic dyes in the presence of silver nanoparticles impregnated core-shell composite microgels, *J. Cleaner Prod.*, 2019, **211**, 855–864, DOI: 10.1016/j.jclepro.2018.11.164.

6 M. A. Bhosale, S. C. Karekar and B. M. Bhanage, Room Temperature Synthesis of Copper Oxide Nanoparticles: Morphological Evaluation and Their Catalytic Applications for Degradation of Dyes and C–N Bond Formation Reaction, *ChemistrySelect*, 2016, **1**, 6297–6307, DOI: 10.1002/slct.201601484.

7 E. Haque, J. W. Jun and S. H. Jhung, Adsorptive removal of methyl orange and methylene blue from aqueous solution with a metal-organic framework material, iron terephthalate (MOF-235), *J. Hazard. Mater.*, 2011, **185**, 507–511, DOI: 10.1016/j.jhazmat.2010.09.035.

8 K. Al-Hamoud, M. R. Shaik, M. Khan, H. Z. Alkhathlan, S. F. Adil, M. Kuniyil, M. E. Assal, A. Al-Warthan, M. R. H. Siddiqui, M. N. Tahir, S. T. Khan, A. A. Mousa and M. Khan, Pulicaria undulata Extract-Mediated Eco-Friendly Preparation of $TiO_2$ Nanoparticles for Photocatalytic Degradation of Methylene Blue and Methyl Orange, *ACS Omega*, 2022, **7**, 4812–4820, DOI: 10.1021/acsomega.1c05090.

9 S. Sarkar, A. Banerjee, U. Halder, R. Biswas and R. Bandopadhyay, Degradation of Synthetic Azo Dyes of Textile Industry: a Sustainable Approach Using Microbial Enzymes, *Water Conserv. Sci. Eng.*, 2017, **2**, 121–131, DOI: 10.1007/s41101-017-0031-5.

10 M. Rafatullah, O. Sulaiman, R. Hashim and A. Ahmad, Adsorption of methylene blue on low-cost adsorbents: A review, *J. Hazard. Mater.*, 2010, **177**, 70–80, DOI: 10.1016/j.jhazmat.2009.12.047.

11 P. O. Oladoye, T. O. Ajiboye, E. O. Omotola and O. J. Oyewola, Methylene blue dye: Toxicity and potential elimination technology from wastewater, *Results Eng.*, 2022, **16**, 100678, DOI: 10.1016/j.rineng.2022.100678.

12 S. Dhananasekaran, R. Palanivel and S. Pappu, Adsorption of Methylene Blue, Bromophenol Blue, and Coomassie Brilliant Blue by α-chitin nanoparticles, *J. Adv. Res.*, 2016, **7**, 113–124, DOI: 10.1016/j.jare.2015.03.003.

13 X. Ren, C. Chen, M. Nagatsu and X. Wang, Carbon nanotubes as adsorbents in environmental pollution management: A review, *Chem. Eng. J.*, 2011, **170**, 395–410, DOI: 10.1016/j.cej.2010.08.045.

14 A. N. Prusov, S. M. Prusova, M. V Radugin and A. V Bazanov, Flax shive as a source of activated carbon for adsorption of methylene blue, *Fullerenes, Nanotubes Carbon Nanostruct.*, 2021, **29**, 685–694, DOI: 10.1080/1536383X.2021.1881063.

15 Y. Ji, F. Xu, W. Wei, H. Gao, K. Zhang, G. Zhang, Y. Xu and P. Zhang, Efficient and fast adsorption of methylene blue dye onto a nanosheet MFI zeolite, *J. Solid State Chem.*, 2021, **295**, 121917, DOI: 10.1016/j.jssc.2020.121917.

16 Y. Liu, W. Zhu, K. Guan, C. Peng and J. Wu, Freeze-casting of alumina ultra-filtration membranes with good performance for anionic dye separation, *Ceram. Int.*, 2018, **44**, 11901–11904, DOI: 10.1016/j.ceramint.2018.03.160.

17 S. R. Geed, K. Samal and A. Tagade, Development of adsorption-biodegradation hybrid process for removal of methylene blue from wastewater, *J. Environ. Chem. Eng.*, 2019, **7**, 103439, DOI: 10.1016/j.jece.2019.103439.

18 C.-Y. Yang, C.-L. Kao and P.-Y. Hung, Preparation of activated carbon from waste cation exchange resin and its application in wastewater treatment, *Carbon Lett.*, 2022, **32**, 461–474, DOI: 10.1007/s42823-021-00275-w.

19 M. Saeed, M. Muneer, A. ul Haq and N. Akram, Photocatalysis: an effective tool for photodegradation of dyes—a review, *Environ. Sci. Pollut. Res.*, 2022, **29**, 293–311, DOI: **10.1007/s11356-021-16389-7**.

20 D. Shao, Y. Zhang, W. Lyu, X. Zhang, G. Tan, H. Xu and W. Yan, A modular functionalized anode for efficient electrochemical oxidation of wastewater: Inseparable synergy between OER anode and its magnetic auxiliary electrodes, *J. Hazard. Mater.*, 2020, **390**, 122174, DOI: **10.1016/j.jhazmat.2020.122174**.

21 L. Qi, K. Zhang, W. Qin and Y. Hu, Highly efficient flow-through catalytic reduction of methylene blue using silver nanoparticles functionalized cotton, *Chem. Eng. J.*, 2020, **388**, 124252, DOI: **10.1016/j.cej.2020.124252**.

22 H. Veisi, S. Azizi and P. Mohammadi, Green synthesis of the silver nanoparticles mediated by Thymbra spicata extract and its application as a heterogeneous and recyclable nanocatalyst for catalytic reduction of a variety of dyes in water, *J. Cleaner Prod.*, 2018, **170**, 1536–1543, DOI: **10.1016/j.jclepro.2017.09.265**.

23 N. Seyedi, K. Saidi and H. Sheibani, Green Synthesis of Pd Nanoparticles Supported on Magnetic Graphene Oxide by Origanum vulgare Leaf Plant Extract: Catalytic Activity in the Reduction of Organic Dyes and Suzuki–Miyaura Cross-Coupling Reaction, *Catal. Lett.*, 2018, **148**, 277–288, DOI: **10.1007/s10562-017-2220-4**.

24 M. Nasrollahzadeh, Z. Issaabadi and S. M. Sajadi, Green synthesis of $Cu/Al_2O_3$ nanoparticles as efficient and recyclable catalyst for reduction of 2,4-dinitrophenylhydrazine, Methylene blue and Congo red, *Composites, Part B*, 2019, **166**, 112–119, DOI: **10.1016/j.compositesb.2018.11.113**.

25 R. Narayanan and M. A. El-Sayed, Catalysis with transition metal nanoparticles in colloidal solution: Nanoparticle shape dependence and stability, *J. Phys. Chem. B*, 2005, **109**, 12663–12676, DOI: **10.1021/jp051066p**.

26 R. Begum, J. Najeeb, A. Sattar, K. Naseem, A. Irfan, A. G. Al-Sehemi and Z. H. Farooqi, Chemical reduction of methylene blue in the presence of nanocatalysts: A critical review, *Rev. Chem. Eng.*, 2020, **36**, 749–770, DOI: **10.1515/revce-2018-0047**.

27 A. S. Altowyan, A. Toghan, H. A. Ahmed, R. A. Pashameah, E. A. Mwafy, S. H. Alrefaee and A. M. Mostafa, Removal of methylene blue dye from aqueous solution using carbon nanotubes decorated by nickel oxide nanoparticles via pulsed laser ablation method, *Radiat. Phys. Chem.*, 2022, **198**, 110268, DOI: **10.1016/j.radphyschem.2022.110268**.

28 B. Wu, Z. Su, Q. Wu, D. H. Kuo, P. Zhang, L. Chen, A. B. Abdeta, M. T. Mosisa, J. Lin, X. Chen and X. Liu, Mn/O co-doped $Bi_2S_3$ bimetal oxysulfide catalyst for highly efficient reduction of organic and hexavalent chromium pollutants in the dark, *Mater. Today Chem.*, 2023, **33**, 101697, DOI: **10.1016/j.mtchem.2023.101697**.

29 P. Zhang, H. Wang, Y. Lai, Y. Xu, L. Chen, Q. Wu, D. H. Kuo, D. Lu, M. T. Mosisa, J. Li, J. Lin and X. Chen, Synergistic Co/S co-doped $CeO_2$ sulfur-oxide catalyst for efficient catalytic reduction of toxic organics and heavy metal pollutants under dark conditions, *J. Water Proc. Eng.*, 2024, **58**, 104820, DOI: **10.1016/j.jwpe.2024.104820**.

30 H. Sun, A. Boke Abdeta, D. H. Kuo, Q. Wu, Y. Guo, O. Ahmed Zelekew, Z. Yuan, J. Lin and X. Chen, Activated carbon supported CuSnOS catalyst with an efficient catalytic reduction of pollutants under dark condition, *J. Mol. Liq.*, 2021, **334**, 116079, DOI: **10.1016/j.molliq.2021.116079**.

31 Q. Wu, P. Zhang, D. H. Kuo, B. Wu, A. B. Abdeta, Z. Su, L. Chen, O. A. Zelekew, J. Lin and X. Chen, Activation of $Cu_3(MoO_4)_2(OH)_2$ with the hydrazine-driven cation reduction into a highly efficient catalyst for the reduction of organic dyes and heavy metals ion, *J. Environ. Chem. Eng.*, 2023, **11**, 109974, DOI: **10.1016/j.jece.2023.109974**.

32 J. Das and P. Velusamy, Catalytic reduction of methylene blue using biogenic gold nanoparticles from Sesbania grandiflora L, *J. Taiwan Inst. Chem. Eng.*, 2014, **45**, 2280–2285, DOI: **10.1016/j.jtice.2014.04.005**.

33 R. Dobrucka, Biofabrication of platinum nanoparticles using Fumariae herba extract and their catalytic properties, *Saudi J. Biol. Sci.*, 2019, **26**, 31–37, DOI: **10.1016/j.sjbs.2016.11.012**.

34 J. Lee, H. Shin, K. S. Choi, J. Lee, J. Y. Choi and H. K. Yu, Carbon layer supported nickel catalyst for sodium borohydride ($NaBH_4$) dehydrogenation, *Int. J. Hydrogen Energy*, 2019, **44**, 2943–2950, DOI: **10.1016/j.ijhydene.2018.11.218**.

35 N. Selvitepe, A. Balbay and C. Saka, Optimisation of sepiolite clay with phosphoric acid treatment as support material for CoB catalyst and application to produce hydrogen from the $NaBH_4$ hydrolysis, *Int. J. Hydrogen Energy*, 2019, **44**, 16387–16399, DOI: **10.1016/j.ijhydene.2019.04.254**.

36 P. K. Singh and T. Das, Generation of hydrogen from $NaBH_4$ solution using metal-boride (CoB, FeB, NiB) catalysts, *Int. J. Hydrogen Energy*, 2017, **42**, 29360–29369, DOI: **10.1016/j.ijhydene.2017.10.030**.

37 P. Hervés, M. Pérez-Lorenzo, L. M. Liz-Marzán, J. Dzubiella, Y. Lub and M. Ballauff, Catalysis by metallic nanoparticles in aqueous solution: Model reactions, *Chem. Soc. Rev.*, 2012, **41**, 5577–5587, DOI: **10.1039/c2cs35029g**.

38 S. H. Gebre, Synthesis and potential applications of trimetallic nanostructures, *New J. Chem.*, 2022, **46**, 5438–5459, DOI: **10.1039/d1nj06074k**.

39 G. Omar, R. G. Abd Ellah, M. M. Y. Elzayat, G. Afifi and H. Imam, Superior removal of hazardous dye using Ag/Au core–shell nanoparticles prepared by laser ablation, *Opt. Laser Technol.*, 2024, **168**, 109868, DOI: **10.1016/j.optlastec.2023.109868**.

40 L. Ma, S. J. Ding and D. J. Yang, Preparation of bimetallic Au/Pt nanotriangles with tunable plasmonic properties and improved photocatalytic activity, *Dalton Trans.*, 2018, **47**, 16969–16976, DOI: **10.1039/c8dt03482f**.

41 Q. Huang, Z. Xi and W. Wei, Controlling synthesis of Au@AgPd core–shell nanocubes and in situ monitoring SERS of their enhanced catalysis, *J. Alloys Compd.*, 2020, **843**, 155971, DOI: **10.1016/J.JALLCOM.2020.155971**.

42 K. E. Alzahrani, A. Aniazy, A. M. Alswieleh, R. Wahab, A. M. El-Toni and H. S. Alghamdi, Antibacterial activity of

trimetal (CuZnFe) oxide nanoparticles, *Int. J. Nanomed.*, 2018, **13**, 77–87, DOI: **10.2147/IJN.S154218**.

43 S. Ge, Y. Zhang, L. Zhang, L. Liang, H. Liu, M. Yan, J. Huang and J. Yu, Ultrasensitive electrochemical cancer cells sensor based on trimetallic dendritic Au@PtPd nanoparticles for signal amplification on lab-on-paper device, *Sens. Actuators, B*, 2015, **220**, 665–672, DOI: **10.1016/j.snb.2015.06.009**.

44 H. J. Lee, D. Hanyu, A. T. N. Dao, H. Kasai, M. Suzuki, H. Yabu, H. Nakatani and K. Kaneko, Controlling the composition and nanostructure of Au@Ag–Pt core@multi-shell nanoparticles prepared by co-reduction method, *Mater. Today Chem.*, 2024, **38**, 102132, DOI: **10.1016/j.mtchem.2024.102132**.

45 C. Sharma, S. Ansari, M. S. Ansari, S. P. Satsangee and M. M. Srivastava, Single-step green route synthesis of Au/Ag bimetallic nanoparticles using clove buds extract: Enhancement in antioxidant bio-efficacy and catalytic activity, *Mater. Sci. Eng., C*, 2020, **116**, 111153, DOI: **10.1016/j.msec.2020.111153**.

46 S. A. Ogundare, T. O. Adesetan, G. Muungani, V. Moodley, J. F. Amaku, O. C. Atewolara-Odule, S. T. Yussuf, N. O. Sanyaolu, A. A. Ibikunle, M. S. Balogun and W. Ewald van Zyl, Catalytic degradation of methylene blue dye and antibacterial activity of biosynthesized silver nanoparticles using Peltophorum pterocarpum (DC.) leaves, *Environ. Sci.: Adv.*, 2022, **2**, 247–256, DOI: **10.1039/d2va00164k**.

47 J. Huang, S. Vongehr, S. Tang, H. Lu, J. Shen and X. Meng, Ag dendrite-based au/ag bimetallic nanostructures with strongly enhanced Catalytic activity, *Langmuir*, 2009, **25**, 11890–11896, DOI: **10.1021/la9015383**.

48 J. Piella, F. Merkoçi, A. Genç, J. Arbiol, N. G. Bastús and V. Puntes, Probing the surface reactivity of nanocrystals by the catalytic degradation of organic dyes: The effect of size, surface chemistry and composition, *J. Mater. Chem. A*, 2017, **5**, 11917–11929, DOI: **10.1039/c7ta01328k**.

49 V. Sharma, N. Sinha, S. Dutt, M. Chawla and P. F. Siril, Tuning the surface enhanced Raman scattering and catalytic activities of gold nanorods by controlled coating of platinum, *J. Colloid Interface Sci.*, 2016, **463**, 180–187, DOI: **10.1016/j.jcis.2015.10.036**.

50 Q. Zhang, T. S. Deng, Y. Q. Dou, M. Z. Wei, S. Li, J. Liu and Z. Cheng, Trimetallic Nanostructures of Silver-Platinum Alloy Shells on Gold Nanorods for Plasmon-Mediated Photocatalysis, *ACS Appl. Nano Mater.*, 2022, **5**, 17048–17058, DOI: **10.1021/acsanm.2c03953**.

51 M. Ding, B. Q. Shan, B. Peng, J. F. Zhou and K. Zhang, Dynamic Pt-$OH^{-}\cdot H_2O$-Ag species mediate coupled electron and proton transfer for catalytic hydride reduction of 4-nitrophenol at the confined nanoscale interface, *Phys. Chem. Chem. Phys.*, 2022, **24**, 7923–7936, DOI: **10.1039/d2cp00673a**.

52 C. Huff, E. Biehler, Q. Quach, J. M. Long and T. M. Abdel-Fattah, Synthesis of highly dispersive platinum nanoparticles and their application in a hydrogen generation reaction, *Colloids Surf., A*, 2021, **610**, 125734, DOI: **10.1016/j.colsurfa.2020.125734**.